

Alexei Kuzmin*, Andris Anspoks, Aleksandr Kalinko, and Janis Timoshenko

The Use of X-ray Absorption Spectra for Validation of Classical Force-Field Models

DOI 10.1515/zpch-2015-0664

Received July 26, 2015; accepted October 11, 2015

Abstract: Extended X-ray absorption fine structure (EXAFS) spectroscopy and molecular dynamics (MD) simulations are two complementary techniques widely used to study the atomic structure of materials. Their combined use, known as the MD-EXAFS approach, allows one to access the structural information, encoded in EXAFS, far beyond the nearest coordination shells and to validate the accuracy of the interaction potential models. In this study we demonstrate the use of the MD-EXAFS method for a validation of several force-field models on an example of the cubic-perovskite SrTiO_3 and hexagonal wurtzite-type ZnO crystals.

Keywords: X-ray Absorption Spectroscopy, EXAFS, Molecular Dynamics, SrTiO_3 , ZnO .

1 Introduction

Classical molecular dynamics (MD) is a modeling tool, which is based on the force-fields and classical Newton's equations of motions for atoms [1–3]. It allows one to examine atomic structure and dynamics of materials at atomic level and nanoscale on time scales up to nanoseconds and more [4]. Moreover, large-scale MD simulations, involving millions of atoms, become feasible nowadays [5, 6].

In multiscale materials modelling the MD method bridges the gap between first-principles simulations and mesoscopic methods, such as coarse-grained MD, kinetic Monte Carlo and dissipative particle dynamics simulations [4, 6]. The classical MD method relies on a description of interactions between atoms using empirical force-field models, parameterized using various analytical forms [7–9].

*Corresponding author: Alexei Kuzmin, Institute of Solid State Physics, University of Latvia, Kengaraga 8, LV-1063 Riga, Latvia, e-mail: a.kuzmin@cfi.lu.lv

Andris Anspoks, Aleksandr Kalinko, Janis Timoshenko: Institute of Solid State Physics, University of Latvia, Kengaraga 8, LV-1063 Riga, Latvia

The choice of the force-field model is determined by the bond type, the desired accuracy, transferability and the computational resources. The accuracy of the force-field model is often a bottleneck of the MD simulation and should be validated by comparing their output with experimental results. Conventionally this is done by a comparison with structural, thermodynamic or vibrational spectroscopic data [2]. However, the restricted amount of available information often prevents reliable selection of the force-field model and also its transferability to nano-sized systems.

In this study we discuss the use of the extended X-ray absorption fine structure (EXAFS) for the validation of the classical force-field models. EXAFS spectra contain information on the local atomic structure in terms of pair and high-order atomic distribution functions and are sensitive to both static and thermal disorder [10–12]. They can be relatively easily measured (also at extreme temperature or pressure conditions) for crystalline, nanocrystalline and disordered materials as well as molecules [13–17]. The time-scale of the photoabsorption process ($\sim 10^{-15} - 10^{-16}$ s) is significantly shorter than the characteristic time ($\sim 10^{-13}$ s) of thermal vibrations. Therefore, the atoms may be considered as frozen at their instantaneous positions during a single photoabsorption process, and the total experimentally measured EXAFS spectrum corresponds to the configurational average of all atomic positions over the time of the experiment. This situation can be straightforwardly modeled combining the MD simulation with the EXAFS calculations, known as the MD-EXAFS approach [18].

The MD simulations have been widely used in the past for the interpretation of EXAFS from disordered [19–25], nanocrystalline [26–30] and crystalline [26, 31–36] materials. Recently, we have proposed that the agreement between the experimental and simulated configuration-averaged EXAFS spectra can be used to validate the accuracy of the force-field models [31, 37, 38]. In this study we will demonstrate this approach for the cubic-perovskite SrTiO_3 and hexagonal wurtzite-type ZnO crystals.

2 MD-EXAFS method

The general scheme of the MD-EXAFS method is shown in Figure 1. First, the structural model of the system should be constructed, taking into account its periodicity, the presence of defects as well as size and shape in the case of nanocrystals and clusters. Second, the suitable force-field potential model should be selected, and its parameters should be provided. Next, the MD simulation at the required temperature and pressure is used to generate a set of instantaneous atomic

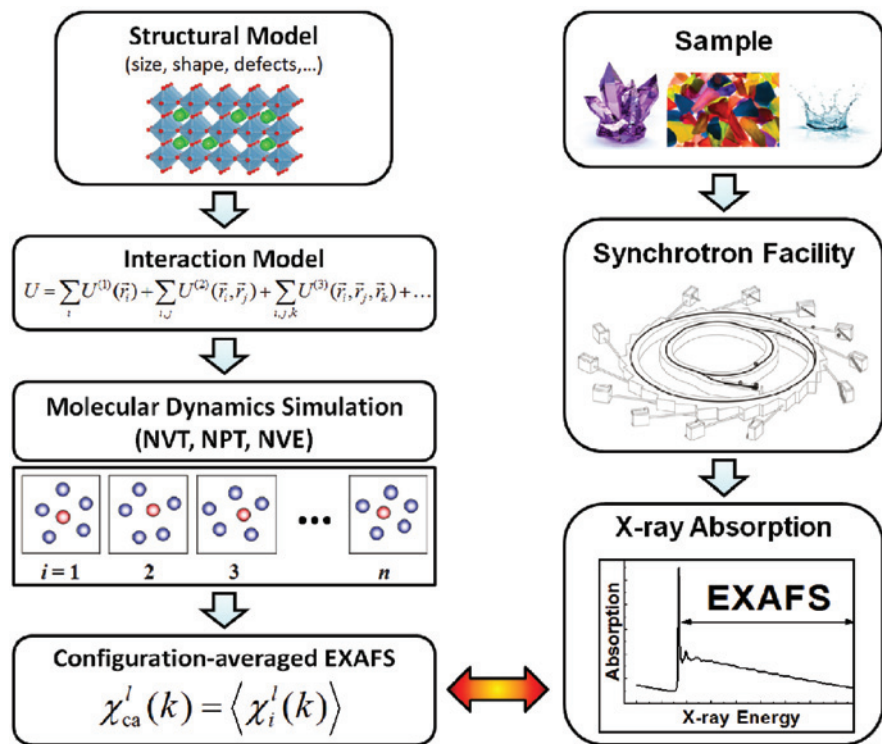


Figure 1: Scheme of the MD-EXAFS approach. See text for details.

configurations ('snapshots' of the material structure), and a set of EXAFS signals is calculated for each of the atomic configurations within the ab initio multiple-scattering approach [12, 39]. Finally, the configuration-averaged EXAFS spectrum is calculated and directly compared with the experimental EXAFS. Note that in such approach both thermal and static disorder effects are naturally accounted within theoretical EXAFS without a need to use any analytical oversimplified models as, for example, harmonic approximation [10].

In this study we consider only the case of classical MD thus neglecting the effect of zero-point vibrations, which become progressively important in the low-temperature limit $T \rightarrow 0$ K [40]. The inclusion of quantum effects can be realized using the path integral implementation of MD (PIMD) [41–43] or Monte Carlo (PIMC) [44] schemes.

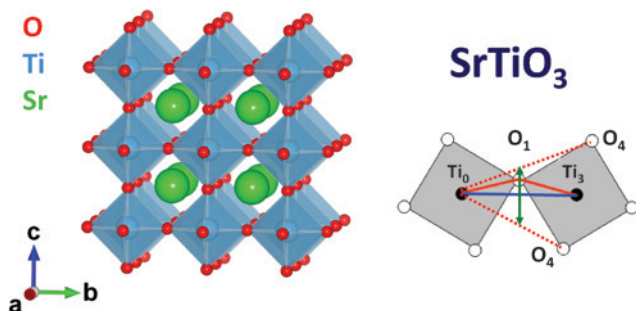


Figure 2: Left panel: fragment of the cubic-perovskite SrTiO_3 crystal structure. Right panel: local environment around Ti_0 atom in SrTiO_3 – the atoms located in the first (O_1), third (Ti_3) and fourth (O_4) coordination shells are shown.

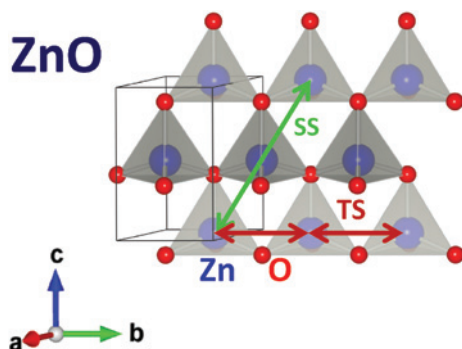


Figure 3: Fragment of the wurtzite- ZnO crystal structure. Scheme of the MD-EXAFS calculations. Two scattering paths, the single-scattering $\text{Zn}_0 \rightleftharpoons \text{Zn}$ ($R = 6.14 \text{ \AA}$) and triple-scattering $\text{Zn}_0 \rightleftharpoons \text{Zn} \rightleftharpoons \text{Zn}$ ($R = 6.50 \text{ \AA}$), are indicated.

2.1 Classical molecular dynamics simulations

Classical MD simulations of cubic SrTiO_3 (Figure 2) and wurtzite ZnO (Figure 3) were performed in the canonical (NVT) ensemble with periodic boundary conditions using the GULP4.0 code [7, 8]. The simulation box was a relaxed supercell with the size equal to $5a_0 \times 5a_0 \times 5a_0$ for SrTiO_3 (space group $Pm\bar{3}m$, $Z = 1$ [45]) and $5a \times 5a \times 3c$ for ZnO (space group $P6_3mc$, $Z = 2$ [46]). The supercells included 625 atoms for SrTiO_3 and 300 atoms for ZnO .

The Newton's equations of motion were integrated with the Verlet leapfrog algorithm [47], with a time step of 0.5 fs. The Nosé-Hoover thermostat [48] was used to keep the average temperature around $T = 300 \text{ K}$ during simulations, corresponding to that of the X-ray absorption experiments [36, 37, 49]. After equilibration during 20 ps, a set of 4000 static atomic configurations was collected during each simulation run with a duration of 20 ps.

Table 1: Buckingham potential parameters (cutoff 15 Å) for SrTiO₃ used in the MD calculations. ε is the sum of the squares of the difference of calculated and experimental EXAFS signals in k -space, shown in Figure 4. The ion charges, used in the Coulomb part of the potential, are also given.

Pair of atoms	A (eV)	ρ (Å)	C (eV Å ⁶)	ε
Wohlwend–Phillpot–Sinnott (WPS) model [51]				0.236
Sr ^{1.331+} –O ^{1.331–}	139621.961934	0.1963	2.33222	
Ti ^{2.662+} –O ^{1.331–}	18476.946631	0.1963	0.0	
O ^{1.331–} –O ^{1.331–}	21943.289277	0.2226	4.14616	
McCoy–Grimes–Lee (MGL) model [52]				0.176
Sr ²⁺ –O ^{2–}	682.172	0.39450	0.0	
Ti ⁴⁺ –O ^{2–}	2179.122	0.30384	8.986	
O ^{2–} –O ^{2–}	9547.960	0.21916	32.0	
Crawford–Jacobs (CJ) model [53]				0.120
Sr ²⁺ –O ^{2–}	1805.2	0.3250	0.0	
Ti ⁴⁺ –O ^{2–}	854.0	0.3770	9.0	
O ^{2–} –O ^{2–}	22764.3	0.1490	20.37	
Sr ²⁺ –Sr ²⁺	9949.1	0.2446	0.0	
Sr ²⁺ –Ti ⁴⁺	12708.1	0.2191	0.00	
Ti ⁴⁺ –Ti ⁴⁺	16963.1	0.1847	0.00	
Thomas–Marks–Begg (TMB) model [54]				0.132
Sr ^{1.84+} –O ^{1.40–}	1769.51	0.319894	0.0	
Ti ^{2.36+} –O ^{1.40–}	14567.40	0.197584	0.0	
O ^{1.40–} –O ^{1.40–}	6249.17	0.231472	0.0	

The two-body, central force, interatomic interactions were described by the force-field models widely used for ionic materials – the Buckingham, Born–Mayer, Morse and Coulomb potentials [8, 50]. Four different parametrization schemes available in the literature were selected for SrTiO₃: the Wohlwend–Phillpot–Sinnott (WPS) model [51], the McCoy–Grimes–Lee (MGL) model [52], the Crawford–Jacobs (CJ) model [53], and the Thomas–Marks–Begg (TMB) model [54]. Three parametrization schemes were chosen for ZnO: the Kulkarni model [55], the Zaoui model [56], and the Wang model [57]. The force-field parameters for SrTiO₃ and ZnO are summarized in Tables 1 and 2, respectively.

2.2 Multiple-scattering EXAFS calculations

Theoretical Ti and Zn K-edge EXAFS spectra $\chi(k)$ (k is the wavenumber) for each atomic configuration, obtained from the MD simulations of SrTiO₃ and ZnO, respectively, were calculated using ab initio real-space multiple-scattering FEFF8

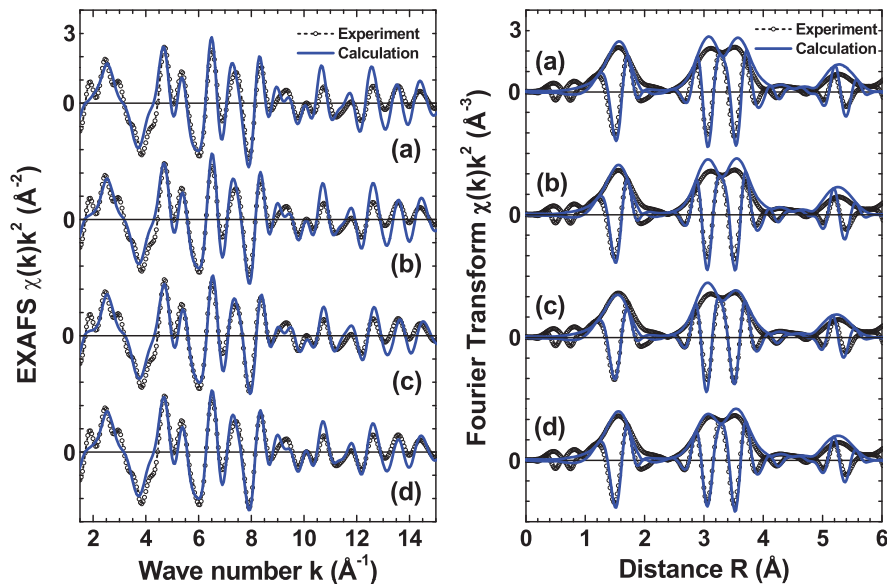


Figure 4: The Ti K-edge EXAFS $\chi(k)k^2$ spectra and their Fourier transforms (modulus and imaginary parts) for cubic-perovskite SrTiO_3 at $T = 300$ K. Open circles – experiment from [49], solid lines – configuration-averaged EXAFS spectra calculated using four force-field models: (a) WPS [51], (b) MGL [52], (c) CJ [53], (d) TMB [54].

Table 2: Potential parameters (cutoff 12 \AA) for wurtzite-ZnO used in the MD calculations. ε is the sum of the squares of the difference of calculated and experimental EXAFS signals in k -space, shown in Figure 5. The ion charges, used in the Coulomb part of the potential, are also given.

		Kulkarni model [55]		$\varepsilon = 0.061$
Buckingham potential	A (eV)	ρ (Å)	C (eV Å ⁶)	
Zn ²⁺ –O ^{2–}	529.7	0.3581	0.0	
O ^{2–} –O ^{2–}	9547.96	0.21916	32.0	
		Zaoui model [56]		$\varepsilon = 0.085$
Buckingham potential	A (eV)	ρ (Å)	C (eV Å ⁶)	
Zn ²⁺ –O ^{2–}	700.3	0.338	0.0	
O ^{2–} –O ^{2–}	22764.0	0.149	27.88	
		Wang model [57]		$\varepsilon = 0.066$
Born–Mayer potential	A (eV)	ρ (Å)		
Zn ^{1.14+} –O ^{1.14–}	257600	0.1396		
Zn ^{1.14+} –Zn ^{1.14+}	78.91	0.5177		
Morse potential	D_e (eV)	a (Å ^{–1})	r_0 (Å)	
O ^{1.14–} –O ^{1.14–}	0.1567	1.164	3.405	

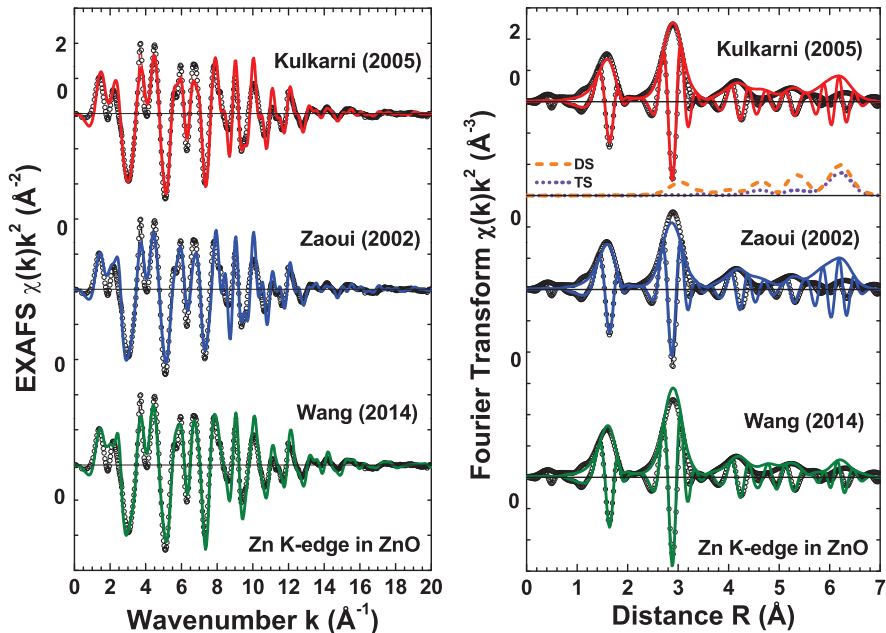


Figure 5: The Zn K-edge EXAFS $\chi(k)k^2$ spectra and their Fourier transforms (modulus and imaginary parts) for wurtzite-ZnO at $T = 300$ K. Open circles – experiment from [37], solid lines – configuration-averaged EXAFS spectra calculated using three force-field models: Kulkarni [55], Zaoui [56] and Wang [57]. The modulus of FTs for the double-scattering (DS) and triple-scattering (TS) contributions are also shown for the Kulkarni model.

code [12, 39]. The calculation of the scattering potential and partial phase shifts was performed within the muffin-tin (MT) approximation (15% overlap of the nearest MT-spheres [39]) only once for the cluster with the radius of 8 \AA , centered at the absorbing metal atom (Ti or Zn) and constructed from the average atomic configuration, which corresponds to the crystallographic structure of the required material [45, 46]. Thus small variations of the cluster potential due to thermal vibrations were neglected.

The multiple-scattering contributions were accounted up to the 7th order to guarantee the convergence of the total EXAFS in the k -space range of interest. The photoelectron inelastic losses were accounted within the one-plasmon approximation employing the complex exchange-correlation Hedin–Lundqvist potential [58]. The value of the amplitude reduction factor S_0^2 was set to 0.67 for SrTiO_3 (as in [49]) and to 1.0 for ZnO (as in [36, 37]).

Finally, the configuration-averaged EXAFS spectra were obtained by averaging over all EXAFS signals evaluated for each atomic configuration independently

and were compared with the experimental Ti and Zn K-edge EXAFS spectra of SrTiO_3 (Figure 4) and ZnO (Figure 5). To quantify the agreement between the experimental and configuration-averaged EXAFS spectra, the sum of the squares of their differences (ϵ) was evaluated in k -space and is reported in Tables 1 and 2. Note that the Fourier transforms (FTs) in Figures 4 and 5 were not corrected for the backscattering phase shift of atoms, therefore the positions of all peaks are displaced to smaller distances relative to their crystallographic values.

3 Results and discussion

3.1 SrTiO_3

The four classical force-field models (WPS [51], MGL [52], CJ [53], and TMB [54]), used here for SrTiO_3 , were developed for different purposes, however they all are based on the Buckingham-type potential.

The WPS model [51] was employed in the simulation of the deposition of SrTiO_3 stoichiometric clusters on single-crystal $\text{SrTiO}_3(001)$ substrate. The set of potential parameters in [51] was adopted from [59] and is able to reproduce experimental lattice constant and elastic properties of bulk SrTiO_3 with the difference of about 0.5% and 28%, respectively. Note that the ion charges are reduced in the WPS model from their formal values to account for bonds covalency.

The MGL model [52] was used to study phase stability and interfacial structures in the SrO-SrTiO_3 system. In spite of the ion charges were set at their formal values, the MGL model reproduces well the bulk lattice constant but fails for the C_{12} elastic constant (about 80% difference).

The intrinsic defect properties of SrTiO_3 at room temperature were studied using the CJ model in [53]. In this model the interaction between cations is additionally taken into account, while employing formal ion charges. The difference between calculated by the CJ model and experimental values of lattice constant and elastic properties for bulk SrTiO_3 are close to that provided by the MGL model [52].

The TMB model [54] was developed for simulating radiation damage in complex $\text{Sr}_{1-3x/2}\text{La}_x\text{TiO}_3$ system. In this case, the ion charges were determined using Mulliken partitioning of ab initio electron density that allowed the authors to reduce the number of free parameters in the model. It was also concluded in [54] that cation-cation Buckingham terms have small effect and, thus, can be excluded. Note that the values of the Mulliken charges are quite close to those of the reduced charges in the WPS model (Table 1).

The configuration-averaged Ti K-edge EXAFS spectra $\chi(k)k^2$ and their FTs for the four models are compared with the experimental data at 300 K in Figure 4. The theoretical model includes the contributions from the nearest six coordination shells (O_1 , Sr_2 , Ti_3 , O_4 , Ti_5 and O_6) around the absorbing titanium atom (Ti_0) (Figure 2). The first peak in FT at 1.5 Å is due to six O_1 atoms forming regular octahedron around Ti_0 ; the second double-peak at 3.5 Å contains contributions from three coordination shells (Sr_2 , Ti_3 , O_4); finally, the last two shells (Ti_5 and O_6) give origin to the third peak at 5.3 Å. The cubic symmetry of $SrTiO_3$ is responsible for the presence of linear atomic chains ($-Ti-O-Ti-$) along the three crystallographic axis (Figure 2), giving rise to strong multiple-scattering effects [60], which influence mainly the second peak in FT. At the same time, a rotation of the TiO_6 octahedra, caused by thermal disorder, destroys dynamically these linear chains by displacing O_1 atoms in the orthogonal direction and also broadens significantly the distribution of O_4 atoms. Both these effects influence mainly the magnitude of the peak at 3.6 Å.

A comparison of the calculated and experimental FTs allows one to make several conclusions. First, all four MD simulations reproduce quite well the first peak at 1.5 Å: the WPS, MGL and TMB models overestimate slightly the rigidity of the Ti–O bonds that results in larger magnitude of the peak, whereas the CJ model is mostly in agreement. The difference between four models becomes clearly visible by looking at peaks corresponding to outer coordination shells: the WPS and MGL models significantly underestimate disorder effects, so that the magnitude of the FT peaks beyond 2.5 Å in the simulations is larger than that in the experiment. The agreement becomes better for the CJ model, however, here the peak at 3 Å, due to mainly Sr_2 atoms, has still larger magnitude in the simulation. Finally, the TMB model seems to provide the best agreement, in spite of some remaining problem with the magnitude of the peak at 3.6 Å. A comparison of the EXAFS spectra for the four models in k -space (see parameter ε in Table 1) indicates that the results of the simulations based on the CJ and TMB models are closest to the experimental data. Taking into account that the number of free force-field parameters is smallest in the TMB model, it can be considered as the best current parametrization for cubic $SrTiO_3$.

3.2 ZnO

Zinc oxide is a key technological material exhibiting semiconducting, piezoelectric and pyroelectric properties [61, 62], which are related to its noncentrosymmetric polar wurtzite-type structure (Figure 3), being stable at ambient conditions. The possibility to produce ZnO with different nanostructured morphologies and

at low cost makes it among the most studied materials [63, 64]. To predict and explain the properties of ZnO nanostructures large scale MD simulations are often required, whose accuracy depends on the reliability of the force-field models. Three popular models [55–57] widely used in the literature are given in Table 2 and will be compared below.

The first two models (Kulkarni [55] and Zaoui [56]) are based on the Buckingham pair potential and formal ion charges. The Kulkarni model [55] was developed with the goal to perform atomistic modeling of ZnO nanostructures and was employed in the simulation of mechanical properties of ZnO nanowires and nanorods [65, 66]. The Zaoui model [56] was used to describe pressure-induced softening of shear modes in wurtzite ZnO.

One of the most recent force-field models for ZnO was developed by Wang et al. [57] with the aim to accurately simulate pressure-induced phase transitions. It incorporates Born–Mayer and Morse potentials and was optimized based on the results of ab initio calculations [57]. The model shows rather good results for a number of ZnO physical properties including the lattice parameters, elastic constants, bulk modulus, structural stabilities, lattice dynamics, and surface energies [57].

The configuration-averaged Zn K-edge EXAFS spectra $\chi(k)k^2$ and their FTs for the three models are compared with the experimental data at 300 K in Figure 5. Good agreement observed in k -space is supported by small difference in the values of ϵ parameter, reported in Table 2. However, a comparison in R -space provides more details on the accuracy of the MD simulations. All three force-field models [55–57] are able to reproduce rather well the behavior of the nearest groups of atoms around the absorbing zinc, which are composed of 4 oxygen atoms in the first coordination shell, 12 zinc atoms at 3.21–3.25 Å, a group of 10 oxygen atoms at about 3.8 Å and 6 zinc atoms at 4.6 Å. These groups of atoms are responsible for the origin of the first three peaks in FT at 1.6 Å, 2.9 Å and 4.1 Å.

The agreement between the calculated and experimental data at longer distances is worse. In particular, there is a small peak at about 4.5–4.8 Å in FTs of the simulated spectra, which is absent in the experimental data. Even larger difference is observed at about 6 Å: here a huge peak is visible in both Kulkarni and Zaoui models, whereas it becomes much smaller but still larger than in the experiment in the Wang model. The magnitude of these two contributions depends strongly on the interference effects between single-scattering (SS) and multiple-scattering (MS) signals as well as on their thermal damping [36]. Detailed analysis [36] shows that the large peak at 6 Å appears due to the interference between the SS signal $\text{Zn}_0 \rightleftharpoons \text{Zn}$ ($R = 6.14$ Å) along the c -axis direction and the MS contribution from $\text{Zn}_0 \rightleftharpoons \text{Zn} \rightleftharpoons \text{Zn}$ ($R = 6.50$ Å) atomic chains along the a - or b -axis direction (Figure 3). The Kulkarni and Zaoui force-field models underestimate the

thermal disorder effect on the MS signal, whereas the Wang model gives better result, which, however, can be still improved.

4 Conclusions

Direct sensitivity of EXAFS to pair and many-atom correlation functions within the range of several nearest coordination shells makes its combination with molecular dynamics simulations, known as the MD-EXAFS method, a natural way for validation of classical force-field models, in addition to conventional structural, thermodynamic or vibrational parameters.

In this study we have demonstrated the use of the MD-EXAFS method for two crystalline materials – cubic-perovskite SrTiO_3 and hexagonal wurtzite-type ZnO , for which a number of force-field models has been developed in the past for different purposes using simple parametrization schemes based on pair interactions [51, 53–57]. The comparison of the simulated configuration-averaged EXAFS signals with the experimental ones in both k - and R -spaces has allowed us to conclude on the accuracy of the force-field models. It is shown that while all considered models reproduce well the average crystallographic structure of the materials, they differ significantly in a description of thermal disorder effects mainly in the outer coordination shells.

Acknowledgement: This work was supported by the Latvian Science Council grant no. 187/2012.

References

1. F. F. Abraham, *Adv. Phys.* **35** (1986) 1.
2. W. E. van Gunsteren and H. J. C. Berendsen, *Angew. Chem. Int. Edit.* **29** (1990) 992.
3. H. Rafii-Tabar, *Phys. Rep.* **325** (2000) 239.
4. T. E. Karakasidis and C. A. Charitidis, *Mater. Sci. Eng. C* **27** (2007) 1082.
5. P. Vashishta, R. K. Kalia, and A. Nakano, *J. Nanopart. Res.* **5** (2003) 119.
6. J. L. Suter, R. L. Anderson, H. C. Greenwell, and P. V. Coveney, *J. Mater. Chem.* **19** (2009) 2482.
7. J. D. Gale, *Philos. Mag. B* **73** (1996) 3.
8. J. D. Gale and A. L. Rohl, *Mol. Simulat.* **9** (2003) 291.
9. M. A. González, *Collection SFN* **12** (2011) 169.
10. P. A. Lee, P. H. Citrin, P. Eisenberger, and B. M. Kincaid, *Rev. Mod. Phys.* **53** (1981) 769.
11. M. Benfatto, C. R. Natoli, and A. Filipponi, *Phys. Rev. B* **40** (1989) 9626.
12. J. J. Rehr and R. C. Albers, *Rev. Mod. Phys.* **72** (2000) 621.

13. J. E. Penner-Hahn, *Coordin. Chem. Rev.* **190–192** (1999) 1101.
14. V. L. Aksenov, A. Yu. Kuzmin, J. Purans, and S. I. Tyutyunnikov, *Phys. Part. Nuclei.* **32** (2001) 675.
15. H. Modrow, *Appl. Spectrosc. Rev.* **39** (2004) 183.
16. S. Bordiga, F. Bonino, K. P. Lillerud, and C. Lamberti, *Chem. Soc. Rev.* **39** (2010) 4885.
17. A. Kuzmin and J. Chaboy, *IUCrj* **1** (2014) 571.
18. A. Kuzmin and R. A. Evarestov, *J. Phys.-Condens. Mat.* **21** (2009) 055401.
19. P. D'Angelo, A. Di Nola, A. Filipponi, N. V. Pavel, and D. Roccatano, *J. Chem. Phys.* **100** (1994) 985.
20. P. J. Merklings, and A. Muñoz-Páez, R. R. Pappalardo, and E. Sánchez Marcos, *Phys. Rev. B* **64** (2001) 092201.
21. D. Cabaret, M. Le Grand, A. Ramos, A.-M. Flank, S. Rossano, L. Galois, G. Calas, and D. Ghaleb, *J. Non-Cryst. Solids* **289** (2001) 1.
22. P. D'Angelo, V. Barone, G. Chillemi, N. Sanna, W. Meyer-Klaucke, and N. V. Pavel, *J. Am. Chem. Soc.* **124** (2002) 1958.
23. Y. Okamoto, *Nucl. Instrum. Meth. A* **526** (2004) 572.
24. F. Farges, Y. Lefrere, S. Rossano, A. Berthereau, G. Calas, and G. E. Brown Jr., *J. Non-Cryst. Solids* **344** (2004) 176.
25. G. Ferlat, J.-C. Soetens, A. San Miguel, and P. A. Bopp, *J. Phys.-Condens. Mat.* **17** (2005) S145.
26. A. Anspoks, A. Kuzmin, A. Kalinko, and J. Timoshenko, *Solid State Commun.* **150** (2010) 2270.
27. A. Anspoks, A. Kalinko, R. Kalendarev, and A. Kuzmin, *Phys. Rev. B* **86** (2012) 174114.
28. S. W. T. Price, N. Zonias, C.-K. Skylaris, T. I. Hyde, B. Ravel, and A. E. Russell, *Phys. Rev. B* **85** (2012) 075439.
29. D. F. Yancey, S. T. Chill, L. Zhang, A. I. Frenkel, G. Henkelman, and R. M. Crooks, *Chem. Sci.* **4** (2013) 2912.
30. A. Anspoks, A. Kalinko, R. Kalendarev, and A. Kuzmin, *Thin Solid Films* **553** (2014) 58.
31. A. Kuzmin and R. A. Evarestov, *J. Phys. Conf. Ser.* **190** (2009) 012024.
32. A. Kalinko, R. A. Evarestov, A. Kuzmin, and J. Purans, *J. Phys. Conf. Ser.* **190** (2009) 012080.
33. J. Timoshenko, A. Kuzmin, and J. Purans, *Centr. Eur. J. Phys.* **9** (2011) 710.
34. A. Kuzmin, V. Efimov, E. Efimova, V. Sikolenko, S. Pascarelli, and I. O. Troyanchuk, *Solid State Ionics* **188** (2011) 21.
35. A. Kalinko and A. Kuzmin, *J. Phys. Conf. Ser.* **430** (2013) 012075.
36. J. Timoshenko, A. Anspoks, A. Kalinko, and A. Kuzmin, *Acta Mater.* **79** (2014) 194.
37. J. Timoshenko, A. Anspoks, A. Kalinko, and A. Kuzmin, *Phys. Status Solidi C* **11** (2014) 1472.
38. K. Lazdins and A. Kuzmin, *IOP C. Ser. Mater. Sci. Eng.* **77** (2015) 012031.
39. A. L. Ankudinov, B. Ravel, J. J. Rehr, and S. D. Conradson, *Phys. Rev. B* **58** (1998) 7565.
40. Y. Yang and Y. Kawazoe, *Europhys. Lett.* **98** (2012) 66007.
41. B. J. Berne and D. Thirumalai, *Ann. Rev. Phys. Chem.* **37** (1986) 401.
42. J. Hutter, M. Iannuzzi, F. Schiffmann and J. VandeVondele, *WIREs Comput. Mol. Sci.* **4** (2014) 15.
43. M. Ceriotti, J. More, D. E. Manolopoulos, *Comput. Phys. Commun.* **185** (2014) 1019.
44. S. a Beccara and P. Fornasini, *Phys. Rev. B* **77** (2008) 172304.
45. S. A. Howard, J. K. Yau, and H. U. Anderson, *J. Appl. Phys.* **65** (1989) 1492.
46. R. R. Reeber, *J. Appl. Phys.* **41** (1970) 5063.
47. R. W. Hockney, *Methods Comput. Phys.* **9** (1970) 136.

48. W. G. Hoover, *Phys. Rev. A* **31** (1985) 1695.
49. M. Vračar, A. Kuzmin, R. Merkle, J. Purans, E. A. Kotomin, J. Maier, and O. Mathon, *Phys. Rev. B* **76** (2007) 174107.
50. N. A. Benedek, A. L. S. Chua, C. Elsässer, A. P. Sutton, and M. W. Finnis, *Phys. Rev. B* **78** (2008) 064110.
51. J. L. Wohlwend, S. R. Phillpot, and S. B. Sinnott, *J. Phys.-Condens. Mat.* **22** (2010) 045001.
52. M. A. McCoy, R. W. Grimes, and W. E. Lee, *Philos. Mag. A* **75** (1997) 833.
53. J. Crawford and P. Jacobs, *J. Solid State Chem.* **144** (1999) 423.
54. B. S. Thomas, N. A. Marks, and B. D. Begg, *Nucl. Instrum. Meth. B* **228** (2005) 288.
55. A. Kulkarni, M. Zhou, and F. Ke, *Nanotechnology* **16** (2005) 2749.
56. A. Zaoui and W. Sekkal, *Phys. Rev. B* **66** (2002) 174106.
57. S. Wang, Z. Fan, R. S. Koster, C. Fang, M. A. van Huis, A. O. Yalcin, F. D. Tichelaar, H. W. Zandbergen, and T. J. H. Vlugt, *J. Phys. Chem. C* **118** (2014) 11050.
58. L. Hedin and B. I. Lundqvist, *J. Phys. C Solid State* **4** (1971) 2064.
59. S. Sekiguchi, M. Fujimoto, M. Nomura, S.-B. Cho, J. Tanaka, T. Nishihara, M.-G. Kang, and H.-H. Park, *Solid State Ionics* **108** (1998) 73.
60. A. Kuzmin, J. Purans, M. Benfatto, and C. R. Natoli, *Phys. Rev. B* **47** (1993) 2480.
61. Z. L. Wang, *J. Phys.-Condens. Mat.* **16** (2004) R829.
62. Ü. Özgür, Ya. I. Alivov, C. Liu, A. Teke, M. A. Reshchikov, S. Doğan, V. Avrutin, S.-J. Cho, and H. Morkoç, *J. Appl. Phys.* **98** (2005) 041301.
63. S. Baruah and J. Dutta, *Sci. Technol. Adv. Mat.* **10** (2009) 013001.
64. A. B. Djurišić, A. M. C. Ng, and X. Y. Chen, *Prog. Quant. Electron.* **34** (2010) 191.
65. A. J. Kulkarni and M. Zhou, *J. Mech. Phys. Solids* **56** (2008) 2473.
66. J. Wang, A. J. Kulkarni, F. J. Ke, Y. L. Bai, and M. Zhou, *Comput. Method. Appl. M.* **197** (2008) 3182.